



Global Biogeochemical Cycles^a



RESEARCH ARTICLE

10.1029/2023GB007702

Special Section:

Understanding carbon-climate feedbacks

Key Points:

- Water stress dominates the interannual variability of terrestrial carbon uptake in the tropics
- The interannual water stress attribution to atmospheric demand is modestly higher than to soil water supply
- The interannual variability of water stress is greater in the wet tropics than in the dry tropics

Supporting Information:

Supporting Information may be found in the online version of this article.

Correspondence to:

P. A. Levine, paul.a.levine@jpl.nasa.gov

Citation:

Levine, P. A., Bloom, A. A., Bowman, K. W., Reager, J. T., Worden, J. R., Liu, J., et al. (2023). Water stress dominates 21st-century tropical land carbon uptake. *Global Biogeochemical Cycles*, *37*, e2023GB007702. https://doi.org/10.1029/2023GB007702

Received 19 JAN 2023 Accepted 14 NOV 2023

© 2023. Jet Propulsion Laboratory, California Institute of Technology. Government sponsorship acknowledged. This is an open access article under the terms of the Creative Commons Attribution-NonCommercial License, which permits use, distribution and reproduction in any medium, provided the original work is properly cited and is not used for commercial purposes.

Water Stress Dominates 21st-Century Tropical Land Carbon Uptake

Paul A. Levine¹, A. Anthony Bloom¹, Kevin W. Bowman¹, John T. Reager¹, John R. Worden¹, Junjie Liu¹, Nicholas C. Parazoo¹, Victoria Meyer¹, Alexandra G. Konings², and Marcos Longo^{1,3}

¹Jet Propulsion Laboratory, California Institute of Technology, Pasadena, CA, USA, ²Department of Earth System Science, Stanford University, Stanford, CA, USA, ³Climate and Ecosystem Sciences Division, Lawrence Berkeley National Laboratory, Berkeley, CA, USA

Abstract Water stress regulates land-atmosphere carbon dioxide (CO₂) exchanges in the tropics; however, its role remains poorly characterized due to the confounding roles of radiation, temperature and canopy dynamics. In particular, uncertainty stems from the relative roles of plant-available water (supply) and atmospheric water vapor deficit (demand) as mechanistic drivers of photosynthetic carbon (C) uptake variability. Using satellite measurements of gravity, CO₂ and fluorescence to constrain a mechanistic carbon-water cycle model from 2001 to 2018, we found that the interannual variability (IAV) of water stress on photosynthetic C uptake was 52% greater than the combined effects of other factors. Surprisingly, the dominance of water stress on C uptake IAV was greater in the wet tropics (94%) than in the dry tropics (26%). Plant-available water supply and atmospheric demand both contributed to the IAV of water stress on photosynthetic C uptake across the tropics, but the IAV of demand effects was 21% greater than the IAV of supply effects (33% greater in the wet tropics and 6% greater in the dry tropics). We found that the IAV of water stress on C uptake was 24% greater than the IAV of the combination of other factors in the net land-atmosphere C sink in the whole tropics, 26% greater in the wet tropics, and 7% greater in the dry tropics. Given the recent trends in tropical precipitation and atmospheric humidity, our findings indicate that water stress—from both -will likely dominate the climate response of land C sink across tropical ecosystems in supply and demandthe coming decades.

Plain Language Summary The amount of carbon that gets absorbed by land ecosystems in the Earth's tropics changes from year to year, and dominates the global carbon dioxide growth rate variability. These changes are related to climate, but it is unclear how much they are driven by water stress relative to other climatic factors. Here, we showed that water stress is responsible for the majority of this variability, not only in the dry tropics, where we would have expected water limitations, but also, surprisingly, in the wet tropics. We found that this variability is driven moderately more by demand from atmospheric aridity than it is by deficits of water in the soil, particularly in the wet tropics. This indicates that water stress will play an important role in the net carbon balance of tropical land ecosystems in a changing climate.

1. Introduction

The interannual variability (IAV) of the atmospheric carbon dioxide ($\rm CO_2$) growth rate has been attributed primarily to the tropical land carbon (C) sink (Jones et al., 2001; Keeling et al., 1995; Rayner et al., 2008; W. Wang et al., 2013; Worden et al., 2021; Zeng et al., 2005). The tropical land surface stores a substantial fraction of global C stocks, both as live biomass (Avitabile et al., 2016; Saatchi et al., 2011) and dead organic matter (Jackson et al., 2017). These ecosystems are highly sensitive to climatic conditions, and year-to-year regional and pan-tropical climate fluctuations, such as El Niño-Southern Oscillation, induce a substantial variation in the net terrestrial $\rm CO_2$ flux (Bowman et al., 2017; Cox et al., 2013; Jung et al., 2017; J. Liu et al., 2017; X. Wang et al., 2014; J. Wang et al., 2016). Understanding IAV in the tropics, therefore, may provide valuable clues regarding the fate of terrestrial ecosystems in a changing climate, and their ability to serve as sources or sinks of atmospheric $\rm CO_2$.

However, there is a considerable uncertainty about the role of water stress on CO₂ flux variability across both wet and dry tropical ecosystems (Humphrey et al., 2018; Jung et al., 2017; Piao et al., 2020; W. Wang et al., 2013;

LEVINE ET AL. 1 of 17

X. Wang et al., 2014; J. Wang et al., 2016; A. Zhang & Jia, 2020). Recent studies indicate that the dry tropics are substantial contributors to recent global net CO₂ flux variability (Ahlström et al., 2015; Fan et al., 2019; Piao et al., 2020; Poulter et al., 2014), in part due to the prominent role of water limitations on photosynthetic C uptake. At the same time, the wet tropics have been found to respond considerably to variable water availability and climate variability (Bowman et al., 2017; Gatti et al., 2014; Green et al., 2020; Palmer et al., 2019; Yang et al., 2018). Furthermore, the wet tropics hold a substantially larger carbon stock (Saatchi et al., 2011), which, if close to a water-induced ecological tipping point (Ahlström et al., 2017; Saatchi et al., 2021), could become a stronger source of atmospheric C under future climate changes. Resolving the sensitivity of tropical ecosystems to water availability is key to understanding the influence of tropical ecosystems within the context of global carbon-climate interactions (Barkhordarian et al., 2021).

Gross primary production (GPP), which is the total uptake of atmospheric CO_2 via photosynthesis, is the dominant component of variability in the net terrestrial carbon balance (Mystakidis et al., 2016; Piao et al., 2020). GPP is fundamentally limited by a number of biotic and abiotic factors, including radiation, leaf area, temperature, soil moisture, and atmospheric aridity (Baker et al., 2021; Bonal et al., 2008; Claessen et al., 2019; Jung et al., 2020; Madani et al., 2020). Specifically, the total impact of water stress on GPP comprises the co-limitations of moisture supply at the soil-root interface and atmospheric demand for moisture at the leaf-atmosphere interface (Bonan et al., 2014; Novick et al., 2016, 2019; Sulman et al., 2016). Therefore, it is important to consider both supply and demand limitations when accounting for the impact of water stress on photosynthetic uptake and, ultimately, net CO_2 fluxes.

In addition, the *relative* importance of supply and demand limitations in the total plant water stress remains a key uncertainty in predicting the tropical carbon sink in upcoming decades. Strong supply side limitations would imply that future tropical GPP will be regulated by water availability (precipitation and, ultimately, soil moisture), while strong limitations due to demand suggest that drivers of evapotranspiration (energy and atmospheric aridity) will play an important role. Under conditions when soil moisture modulates surface atmospheric temperature and humidity, the feedbacks between supply and demand can become as impactful as the individual components, particularly in the tropics (Green et al., 2019; Humphrey et al., 2021). These feedbacks may be modulated by strategies developed by plants to minimize the risk of stress-induced mortality and leaf loss by regulate leaf stomatal openings—and consequently photosynthetic uptake—to reduce transpiratory water fluxes (Grossiord et al., 2020; Sperry et al., 2017).

At a process level, terrestrial ecosystem models have long accounted for water supply and demand limitations (Bonan et al., 2014; Trugman et al., 2018), but these parameterizations introduce uncertainty at coarser scales, particularly when based on plant functional types (PFTs) which are unable to account for hydroclimatic and edaphic conditions that lead to unique, emergent behavior of terrestrial ecosystems (Konings & Gentine, 2017). Here, we inform these parametric uncertainties with spatially explicit data from multiple Earth observation satellites spanning multiple decades, using the CARbon DAta-MOdel fraMework (CARDAMOM), a model-data fusion system that constrains a simple ecosystem model with observations terrestrial carbon and water states and fluxes (Bloom & Williams, 2015; Bloom et al., 2016, 2020; Quetin et al., 2020; Yang et al., 2021; Yin et al., 2020). Bloom et al. (2020) recently extended the process model within CARDAMOM to include a mechanism for water supply to limit GPP. They demonstrated that with this mechanism, their reanalysis was able to capture the drought response of observationally constrained terrestrial CO₂ fluxes in the tropics. Furthermore, the drought response could be further resolved into both the instantaneous effects of water supply limitations on photosynthesis, and the subsequent effects resulting from shifts in the ecosystem state (Bloom et al., 2020). Here, for the first time, we assimilate terrestrial water storage anomalies from the Gravity Recovery and Climate Experiment (GRACE) (Wiese et al., 2016) as a constraint on the CARDAMOM model water states (see Section 2.2 for details). In addition to the GPP water supply limitation (as in Bloom et al. (2020) and Yang et al. (2021)), we extend the process model in CARDAMOM to include an atmospheric water demand limitation on GPP, specifically via vapor pressure deficit (VPD, see Section 2.1 for details). With these developments, we used CARDAMOM to obtain a reanalysis of the coupled carbon and water cycles, constrained by satellite observations of carbon and water states and fluxes, in order to diagnose the IAV of water stress on tropical carbon fluxes in the first two decades of the 21st century.

Understanding the interannual sensitivities of tropical ecosystems to water stress—namely the co-limitations of water demand and supply on photosynthetic C uptake—is critical to advancing understanding of (a) soil

LEVINE ET AL. 2 of 17

- 1. How much does water stress contribute to the IAV of carbon uptake (GPP) at continental and pan-tropical scales?
- 2. How much do the instantaneous effects of water limitations to GPP contribute to the IAV of the net carbon balance?
- 3. How much of the IAV in water stress is the result of limitations from soil water supply versus those from atmospheric demand?

2. Methods and Data

Section 2.1 describes the ecosystem model used within the CARDAMOM framework, and explains its water stress parameterizations. Section 2.2 summarizes how we assimilated multiple satellite observations and derived data products into the CARDAMOM framework, and details our recently developed method for including GRACE as a constraint on water storage. Section 2.3 describes how we leveraged the observationally constrained monthly reanalysis to distinguish between (a) water stress and (b) the combination of all other factors driving the variability of C uptake.

2.1. Modeling Water Stress

CARDAMOM is a model-data fusion system designed to assimilate multiple sources of observational data into a parsimonious model that represents the states and fluxes of the terrestrial carbon and water cycles. We used the Data-Assimilation Linked Ecosystem C (DALEC) model (Williams et al., 2005), which has been used extensively within CARDAMOM to diagnose terrestrial C cycle dynamics across a range of site-level and spatially resolved approaches (Bloom & Williams, 2015; Bloom et al., 2016, 2020; Quetin et al., 2020; Yang et al., 2021; Yin et al., 2020). The specifics of DALEC have been described extensively by Bloom et al. (2020), to which we refer the reader for a complete description of the model. The CARDAMOM framework, namely DALEC model states and processes, observational constraints and forcing data sets are summarized in Figure S1 of the Supporting Information S1.

Bloom et al. (2020) introduced a representation of water stress into DALEC—in the form of a commonly used " β " approach (Trugman et al., 2018)—in which GPP is calculated in two sequential steps: First, the Aggregated Canopy Model (ACM) (Williams et al., 1997) is used to calculate how much GPP would be expected under conditions of no water stress, that is, a saturated rooting-zone soil and canopy airspace. This quantity—henceforth abbreviated as $\text{GPP}_{pot}(t)$ —is a function of radiation, temperature, leaf area, and atmospheric CO_2 concentrations at time t; therefore GPP_{pot} represents time-varying non-water stress limitations on GPP, such as wet-to-dry season variability in downward radiation or leaf area variability in deciduous ecosystems.

Subsequently, actual GPP is calculated as the product of $GPP_{pot}(t)$ and a water stress scaling factor, $\beta_{paw}(t)$, which is defined as

$$\beta_{paw}(t) = \begin{cases} \frac{PAW(t)}{PAW_{wp}}, & \text{if } PAW(t) < PAW_{wp} \\ 1, & \text{if } PAW(t) \ge PAW_{wp} \end{cases}$$
 (1)

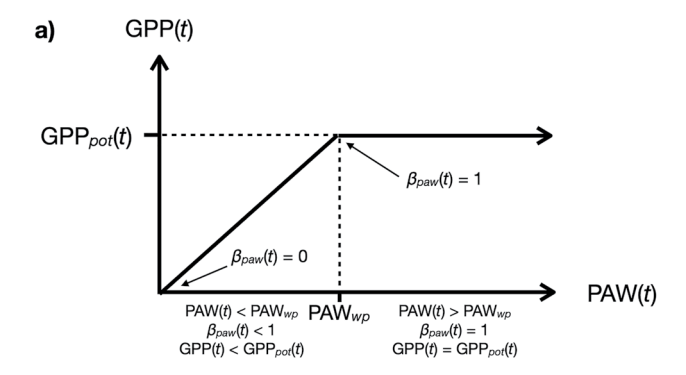
in which PAW(t) is the prognostic plant-available water (PAW) state and PAW_{wp} is a time-invariant, CARDAMOM-optimized parameter representing a conceptual threshold below which GPP linearly reduces to zero along with PAW (Figure 1a). Here, we introduced an additional scaling factor, $\beta_{vpd}(t)$, to account directly for VPD limitations at time t that are independent of PAW as

$$\beta_{vpd}(t) = \begin{cases} 1 - \left(\frac{\text{VPD}(t)}{\text{VPD}_{\text{max}}}\right)^b, & \text{if VPD}(t) < \text{VPD}_{\text{max}} \\ 0, & \text{if VPD}(t) \ge \text{VPD}_{\text{max}} \end{cases}$$
(2)

LEVINE ET AL. 3 of 17

19449224, 2023, 12, Downloaded from https:

/10.1029/2023GB007702 by Stanford University, Wiley Online Library on [27/01/2024].



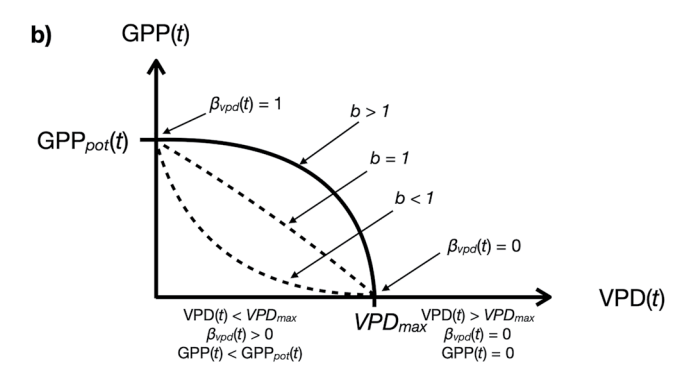


Figure 1. Water stress functions in DALEC based on limitations from plant available water (a) and vapor pressure deficit (b).

where $\mathrm{VPD}_{\mathrm{max}}$ and b are optimized parameters in a function (Figure 1b) designed to approximate the range of hypothesized responses of GPP stress to VPD (Grossiord et al., 2020; Leuning, 1995), and VPD is calculated using 2-m air temperature and dewpoint temperature from the ERA-Interim forcing data. The overall GPP is calculated as

$$GPP = \beta_{paw} \beta_{vpd} GPP_{pot}. \tag{3}$$

2.2. Data Assimilation

CARDAMOM uses an iterative Bayesian framework to optimize the parameters and initial states of DALEC based on multiple streams of observations and derived data products (Bloom & Williams, 2015; Bloom et al., 2016). Here, we conducted a pan-tropical ($30^{\circ}S-30^{\circ}N$) CARDAMOM analysis at a resolution of 4° latitude \times 5° longitude, following the same approach and using the same observational data and uncertainties as Bloom et al. (2020), aside from three exceptions described below. The complete set of observation and associated uncertainties is shown in Table S1 of the Supporting Information S1; the uncertainty choices and their implications on our results are discussed in Section 3.4.

The first exception is that in place of the solar induced fluorescence (SIF) product from the Greenhouse Gas Observing Satellite (GOSAT) as used in Bloom et al. (2020), we obtained estimates of SIF from the contiguous SIF (CSIF) product (Y. Zhang et al., 2018), which is a continuous 2001–2018 SIF product trained on Orbiting Carbon Observatory-2 (OCO-2) data along with longer-spanning ancillary data sets; because SIF is not a direct measurement of GPP, we follow the approach of MacBean et al. (2018) and Bloom et al. (2020), in which SIF and GPP are both normalized by their temporal

mean values so that SIF only informs the temporal variability of GPP. The second exception is that we constrain the temporal mean of CARDAMOM GPP using the FluxCom 2001–2014 GPP product (Jung et al., 2019): for lack of specific knowledge on decadal time-averaged FluxCom GPP product accuracy, we opted for an uncertainty factor of 1.05 (approximately $\pm 5\%$, see Table S1 in Supporting Information S1), as we found that larger GPP uncertainty choices led to substantial and systematic inconsistencies in the spatial patterns between the CARDAMOM and FluxCom time-averaged GPP values.

The third exception is a significant development to the CARDAMOM framework that allows it to assimilate terrestrial water storage anomalies—available from 2003 to 2016 from GRACE—as a constraint on water storage in DALEC: the constraint on terrestrial water storage was achieved by (a) adopting the development of Yang et al. (2021), which appends the Bloom et al. (2020) formulation of PAW to include a second prognostic plant unavailable water (PUW) pool, and (b) expanding the CARDAMOM cost function of Bloom et al. (2020) to include the GRACE constraint (Wiese et al., 2016). In contrast to PAW, PUW represents water that is inaccessible to plant roots but still part of the total water balance. The sum of PAW and PUW pool represents total water storage within the land surface and subsurface, in mm of equivalent water thickness; as a result, temporal changes in PAW and PUW are directly comparable to the total water storage anomalies (TWSA) provided by GRACE. Specifically, for each monthly GRACE TWSA observation (TWSA $_0(t)$), an equivalent monthly DALEC model TWSA (TWSA $_m(t)$) is calculated as follows:

$$TWSA_m(t) = PAW(t) + PUW(t) - \sum_{t=1}^{N} \frac{PAW(t) + PUW(t)}{N}$$
(4)

where PAW(t) and PUW(t) are the monthly PAW and PUW water states concurrent with the GRACE observations in month t, and N is the number of months in the observational record. This ensures that the modeled and observed TWSA are relative to a mean value from the same set of months. We then calculate the likelihood of the DALEC model TWSA, \mathcal{L}_{TWSA} , as follows:

$$\mathcal{L}_{TWSA} = \exp\left(-\frac{1}{2} \sum_{t=1}^{N} \frac{\left(TWSA_{m}(t) - TWSA_{O}(t)\right)^{2}}{\sigma^{2}}\right). \tag{5}$$

LEVINE ET AL. 4 of 17

We prescribe a ± 50 mm observation uncertainty ($\sigma = 50$ mm) for TWSA, which conservatively represents GRACE error estimates (Wiese et al., 2016).

With the previously mentioned exceptions of the SIF product substitution, the mean GPP constraint, and the addition of the GRACE constraint, we otherwise assimilated the same set of observational data used by Bloom et al. (2020) (see Data Availability Statement for details on all data sources). This includes data from (a) the National Aeronautics and Space Administration's Carbon Monitoring System Flux (CMS-Flux), which assimilates satellite observations of carbon to infer grid-scale net carbon fluxes from 2010 to 2018 (J. Liu et al., 2014, 2021), (b) mean biomass estimates from the Geoscience Laser Altimeter System (GLAS) (Saatchi et al., 2011), (c) leaf area index from the Moderate-resolution Imaging Spectroradiometer (MODIS) (Myneni et al., 2015), from which we assimilated only the mean LAI due to seasonal LAI retrieval biases (Bi et al., 2015), (d) soil organic carbon (SOC) from the Harmonized World Soil Database (HWSD) for the year 2001 (Köchy et al., 2015), and (e) mean fire C emissions from 2001 to 2015 from the inversion estimates of Worden et al. (2017) (see Table S1 in Supporting Information S1 for details).

We forced DALEC with monthly temperature, humidity, radiation, and precipitation from the European Center for Medium Range Forecasting Interim (ERA-Interim) reanalysis (Berrisford et al., 2011), burned area from the Global Fire Emissions Database (GFED4) (Randerson et al., 2017), and atmospheric CO_2 concentrations from the National Oceanic and Atmospheric Administration's Earth System Research Laboratories (Dlugokencky & Tans, 2020). Monthly forcing and observational data were regridded to a common resolution of 4° latitude \times 5° longitude from 30°S to 30°N. Parameters and initial conditions were optimized independently at each grid cell using an adaptive Metropolis Hastings Markov Chain Monte Carlo to sample 4,000 solutions from the posterior distribution (see Bloom and Williams (2015) and Bloom et al. (2020) for details). As highlighted by Bloom et al. (2020) and J. Liu et al. (2017), there are substantial spatial error covariances between $4^\circ \times 5^\circ$ pixels due to the effectively coarser (continental-scale) information content of the inversion-based CO_2 -flux estimates. To mitigate the impact of these errors on our analysis, we conduct the analysis of water stress variability (Section 2.3) to (a) 6 hemi-continental regions, (b) the dry tropics and wet tropics, and (c) the pan-tropical study domain.

To quantitatively evaluate the updated DALEC model structure's ability to reproduce and independently predict seasonal and interannual variations in tropical C fluxes, we (a) evaluate the timing and amplitude of monthly CARDAMOM GPP, NBP, and TWS anomalies against the corresponding assimilated observations (CSIF, CMS-Flux, and GRACE, respectively, where and when these are available), and (b) perform a dedicated training/validation experiment based on the Bloom et al. (2020) approach, where we only use 2001–2015 observation data and evaluate the CARDAMOM skill in predicting 3 years of withheld 2016–2018 NBP data. The timing and amplitude comparison provides an evaluation of the model skill in representing the observation timing and amplitude throughout the 2001–2018 time period; for each quantity, we use the standard deviation of the 2001–2018 time series as an integrated measure of observed and modeled variable amplitude, and we use the Pearson's correlation coefficient (henceforth abbreviated as r) as an integrated measure of timing consistency between the two signals. The dedicated training/validation experiment provides an evaluation of the process model skill in representing the integrated land-atmosphere CO_2 flux in the absence of observational constraints. For both evaluation steps, we conduct both full monthly data and de-seasonalized anomaly comparisons (see Section 2.3 for de-seasonalized anomaly derivation).

2.3. Analysis of Water Stress Variability

To diagnose the relative contribution of water stress to the temporal variability of GPP, we first decompose the GPP variability into (a) the GPP component attributable to water stress, and (b) the GPP component attributable to all other drivers of GPP variability. Decomposing GPP into component terms was facilitated by the water stress formulation of DALEC described in Equation 3, as GPP_{pot} already represents all factors affecting GPP other than water stress. We can then define the GPP "deficit" (GPP_{def}) , in parallel with a similar concept based on evapotranspiration (Stephenson, 1998), as

$$GPP_{def}(t) = GPP(t) - GPP_{pot}(t).$$
(6)

Here, GPP_{def} represents the additional GPP that could be attained instantaneously in the absence of water stress, but does not account for synchronous or delayed feedbacks to the ecosystem, such as changes to leaf area or plant mortality. By rearranging Equation 6 as

LEVINE ET AL. 5 of 17

$$GPP(t) = GPP_{pot}(t) - GPP_{def}(t), \tag{7}$$

we have divided GPP into the two component time series, with $-GPP_{def}$ representing the contribution of water stress to GPP variability, and GPP_{pot} representing the contribution of everything else, that is, radiation, temperature, and leaf area.

To further assess the variability of water stress within the context of net land-atmosphere CO_2 fluxes, we examined the effect of GPP_{def} on the net biosphere production (NBP), defined as uptake from GPP minus C losses due to respiration and disturbance (where a positive value represents a net land-atmosphere CO_2 uptake). We derived the "potential" NBP (NBP_{pot}) that represents the net CO_2 flux in the absence of instantaneous GPP water limitations as $NBP_{pot} = NBP + GPP_{def}$ which we then rearrange as

$$NBP = NBP_{pot} - GPP_{def}. (8)$$

We further partitioned GPP_{def} into two terms corresponding to limitations due to insufficient supply of plant available water (GPP^{paw}_{def}) and limitations due to excessive demand from atmospheric VPD (GPP^{vpd}_{def}) so that

$$GPP_{def} = GPP_{def}^{paw} + GPP_{def}^{vpd}$$
(9)

where we define GPP_{def}^{paw} as

$$GPP_{def}^{paw} = GPP_{def} \left(\frac{1 - \beta_{paw}}{(1 - \beta_{paw}) + (1 - \beta_{vod})} \right)$$

$$\tag{10}$$

in order to distribute interactions proportionately between the two terms. Note that β_{paw} is large when the deficit associated with PAW is small; we therefore weight by $1 - \beta_{paw}$ instead of by β_{paw} . We similarly define GPP $_{def}^{vpd}$ as

$$GPP_{def}^{vpd} = GPP_{def} \left(\frac{1 - \beta_{vpd}}{(1 - \beta_{paw}) + (1 - \beta_{vpd})} \right). \tag{11}$$

To isolate the inter-annual variations from the seasonal component of each flux term in Equations 7–9, we first subtract the mean 2001–2018 seasonal cycle as follows:

$$\Delta F_{i,j} = F_{i,j} - \frac{1}{N} \sum_{k=0}^{N-1} F_{i,k}$$
 (12)

where $F_{i,j}$ is the carbon flux term—namely GPP, GPP_{def}, GPP_{pot}, GPP^{vpd}_{def}, GPP^{paw}_{def} and NBP_{pot}—at month = i and year = j, and N is the number of years (N = 18), and $\Delta F_{i,j}$ represents the de-seasonalized anomaly; henceforth, for each flux, we denote the de-seasonalized anomalies as Δ GPP, Δ GPP_{def}, Δ GPP_{pot}, Δ NBP_{pot}, Δ GPP^{vpd}_{def}, and Δ GPP^{paw}_{def}, respectively. We derived regional estimates of each de-seasonalized flux by (a) calculating the mean CARDAMOM flux at each grid cell, (b) regionally aggregating area-weighted fluxes across each region, and (c) de-seasonalizing regional time-varying fluxes using Equation 12. We then summarize the 2001–2018 inter-annual variability (IAV) as the standard deviation of the monthly de-seasonalized anomalies, and denote these as $\sigma\Delta$ GPP, $\sigma\Delta$ GPP_{def}, $\sigma\Delta$ GPP_{pot}, $\sigma\Delta$ G

3. Results and Discussion

3.1. Evaluation of CARDAMOM Carbon-Water Reanalysis

Overall, the CARDAMOM modeled GPP, TWSA and NBP (Figure 2) are in broad agreement with the corresponding observations of SIF, GRACE TWSA and CMS-Flux NBP across the six hemi-continental regions (Table 1): we find all correlations are positive and significant (with p-value <0.05) between GPP and SIF (r = 0.32–0.95), terrestrial water storage anomalies (r = 0.82–0.97) and NBP (r = 0.56–0.95). We also find broad consistency between the amplitudes of 2001–2018 NBP, TWSA and relative amplitudes of GPP, and the corresponding observation amplitudes (Table 1 and Figure 2): across the six hemi-continental regions, the ratio of modeled-to-observed amplitudes for the full monthly data timeseries span 0.61–1.38 across all observational data sets. On a pantropical scale, the FluxCom time-averaged GPP (86.7 PgC/y) is within the range of CARDAMOM

LEVINE ET AL. 6 of 17

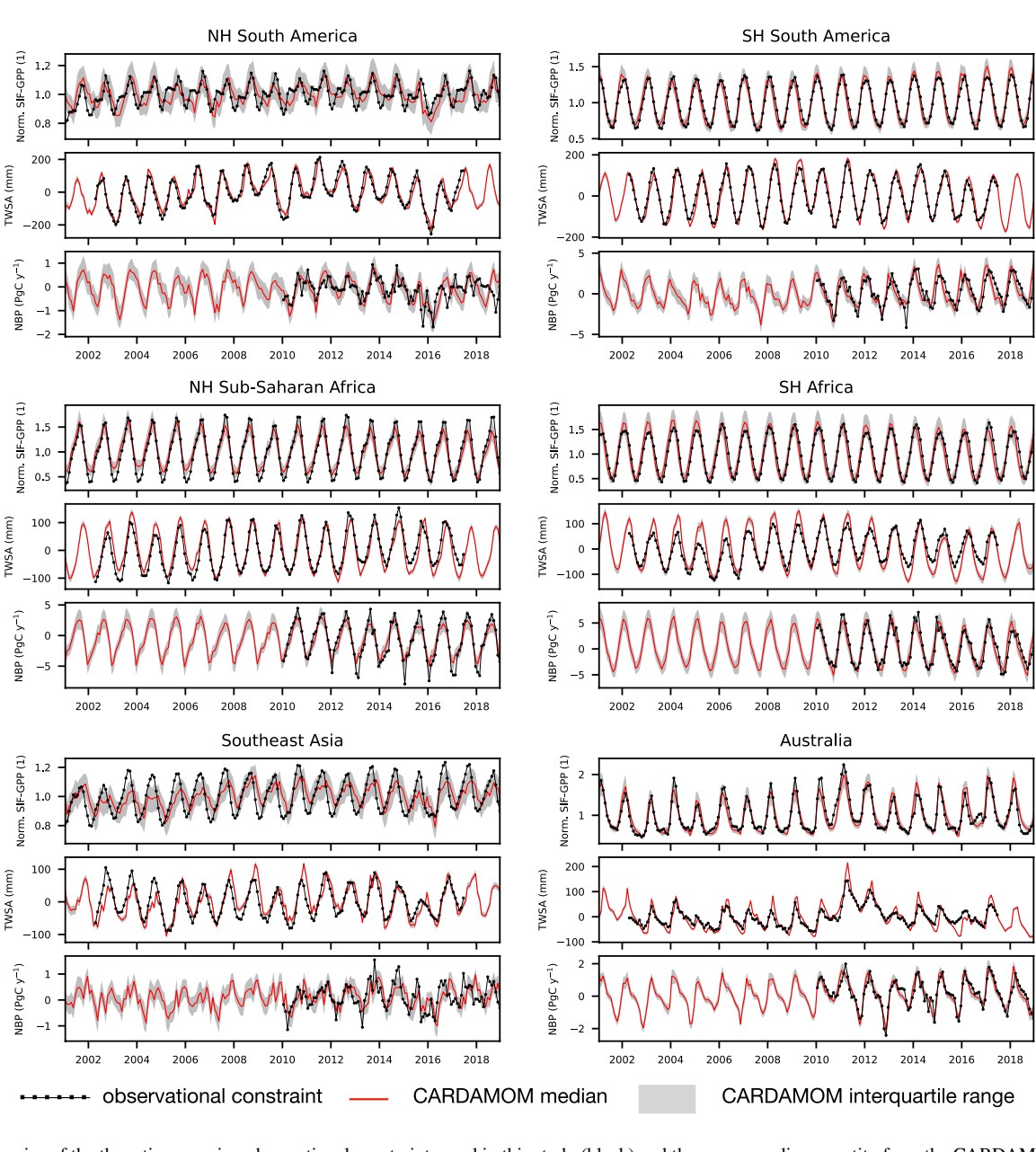


Figure 2. Time series of the three time-varying observational constraints used in this study (black) and the corresponding quantity from the CARDAMOM posterior distribution (red) across the six hemi-continental regions used in the analysis. The top row of each panel shows SIF from CSIF and GPP from CARDAMOM, both divided by their time mean. The second row of each panel shows the total water storage anomaly (TWSA) from GRACE and CARDAMOM, both with their time mean removed. The normalizations of SIF and TWSA data (along with the corresponding CARDAMOM quantities in each panel) illustrate the transformations necessary for the assimilation for CSIF and GRACE (see Section 2.2). The bottom row of each panel shows NBP from CMS-Flux and CARDAMOM. The model-data fit correlation metrics and standard deviation ratios are reported in Table 1.

2001–2018 time-averaged GPP (IQR = 74.3–93.8 PgC/y), and mean grid-scale CARDAMOM GPP values (Figure S3 in Supporting Information S1) are in broad agreement with the corresponding FLUXCOM GPP values (r = 0.94; p-value < 0.05). We find that in the two wetter regions–NH South America and SE Asia–show the lowest consistency in terms of the timing of GPP and SIF (r = 0.42 and r = 0.32 respectively); we note that in both regions the observation and model normalized dynamical ranges are relatively lower (normalized SIF and GPP standard deviation span 7%–11%, see Figure 2) relative to other regions, where the dynamical ranges of normalized GPP and SIF are considerably larger (normalized SIF and GPP standard deviation $\geq 25\%$). We speculate that the relatively lower variability could either (a) be a limitation in the sensitivity of CSIF predictors to relatively small changes in GPP, (b) a limitation in the CARDAMOM structure for representing relatively small

LEVINE ET AL. 7 of 17

Table 1

Correlation Coefficients (r) Between Assimilated Observations and CARDAMOM Posterior Mean Across Six Hemi-Continental Regions (Time Series Illustrated in Figure 2) and the Corresponding Metrics for De-Seasonalized Observations and CARDAMOM Posterior Mean (Time Series Illustrated in Figure S2 of the Supporting Information S1)

	Full monthly data $r\left(\sigma_{M}/\sigma_{O}\right)$			Deseasonalized anomalies $r(\sigma_{M}/\sigma_{O})$		
	SIF/GPP	TWSA	NBP	SIF/GPP	TWSA	NBP
NH South America	0.42* (0.95)	0.94* (0.91)	0.62* (1.10)	0.29* (1.34)	0.90* (0.87)	0.74* (0.71)
SH South America	0.92* (1.06)	0.97* (1.08)	0.79* (1.04)	0.38* (1.16)	0.77* (1.11)	0.43* (0.95)
NH Sub-Saharan Africa	0.88* (0.74)	0.91* (1.03)	0.95* (0.74)	0.03 (1.26)	0.08 (0.61)	0.45* (0.51)
SH Africa	0.95* (1.04)	0.89* (1.34)	0.92* (1.01)	0.15* (1.07)	0.30* (0.95)	0.29* (0.56)
Southeast Asia	0.32* (0.61)	0.82* (1.03)	0.56* (0.84)	0.57* (1.15)	0.51* (1.28)	0.62* (0.74)
Australia	0.79* (0.98)	0.91* (1.38)	0.91* (1.03)	0.69* (0.71)	0.88* (1.26)	0.70* (0.93)
Tropics	0.34* (1.31)	0.81* (1.14)	0.41* (0.95)	0.23* (0.71)	0.79* (1.13)	0.52* (0.56)
Wet Tropics	0.05 (0.60)	0.81* (0.91)	0.53* (0.67)	0.15* (0.96)	0.66* (0.90)	0.55* (0.61)
Dry Tropics	0.70* (1.20)	0.74* (1.27)	0.59* (0.95)	0.36* (0.60)	0.84* (1.16)	0.40* (0.51)

Note. The asterisks denote the statistical significance of r with p-value < 0.05. The bracketed numbers denote the ratio of CARDAMOM posterior mean standard deviation (σ_M) versus observation standard deviation (σ_O), where and when observations are available (see Figure 2).

wet tropical seasonal variations, and/or (c) a limitation in the CARDAMOM cost function sensitivity to small relative GPP variations. On a pan-tropical scale, we generally find consistency between observation and model amplitudes (0.60–1.31), however correlations span lower values (Table 1), and in particular we find no significant correlation between wet tropical modeled GPP and observed SIF across the entirety of the wet tropics (r = 0.05; p-value > 0.05); the reduced correlations on pantropical scales are generally expected as the inter-hemisphere and inter-continental compensation effects of seasonal cycles can amplify model-data inconsistencies from individual hemi-continental regions.

On a de-seasonalized basis, monthly anomalies modeled by CARDAMOM are broadly in agreement with the equivalent observations (Figure S2 in Supporting Information S1; Table 1). Relative to the full monthly timeseries, we find lower yet positive and significant correlations for GPP, TWSA, and NBP (against the corresponding de-seasonalized observations) across the six hemi-continental regions, with the exception of NH Sub-Saharan Africa, were correlations are positive but not significant for GPP and TWSA (see Table 1), and a modestly broader range of modeled-to-observed ratios in the de-seasonalized variability (0.71-1.34, 0.61-1.28, and 0.51-0.95). We find a notable model-data mismatch between SIF and GPP in Northern Hemisphere South America region during the 2015–2016 El Niño (Figure S2 in Supporting Information S1); however, we find that the model NBP is consistent with the CMS-Flux NBP, which in itself represents both GPP and gross land-atmosphere C losses. The lack of simultaneous model consistency with joint GPP and NBP constraints on an inter-annual basis could be attributable to (a) limited sensitivity of the CSIF product to wet tropical ecosystem drought, and/or (b) limitations in the CARDAMOM representations of combined NBP and GPP drought responses. On a pantropical basis, we find de-seasonalized anomaly amplitudes are broadly consistent with assimilated data sets (de-seasonalized variability ratios span 0.51-1.13), and correlations are all significant albeit generally lower than the hemi-continental values (Table 1); similarly to the full monthly data sets, we expect hemispherical and continental compensation explains the modest degradation of amplitude and correlation skill across pantropical scales.

In the dedicated training/validation experiment, we find broad monthly model-observation consistency during the 2010–2015 training period for all hemi-continental regions (r = 0.54–0.95; Table 2) with root-mean-square error values approximately an order of magnitude smaller than the seasonal NBP variability. With the exception of NH Sub-Saharan Africa, we find a modest degradation of correlation during the 2016–2018 validation period (r = 0.18–0.93); and a modest increase in the corresponding RMSE values.

Overall, the CARDAMOM model structure used in this study can (a) skillfully represent the timing and variability of observation-based GPP, TWSA, and NBP estimates (Table 1), and (b) adequately predict NBP variability during a prediction period (2016–2018), relative to training period performance (2010–2015; Table 2). The limitations of modeled variables, observational constraints and the broader implications of model-data mismatches are further discussed in Section 3.4.

LEVINE ET AL. 8 of 17

19449224, 2023, 12, Downloaded from https://agupubs.onlinelibrary.wiley.com/doi/10.1029/2023GB007702 by Stanford University, Wiley Online Library on [27/01/2024]. See the Terms and

conditions) on Wiley Online Library for rules of use; OA articles are governed by the applicable Creati

Validation of CARDAMOM Framework Against Assimilated and Withheld Data for the Assimilation/Prediction Sensitivity Experiment (See Section 2.2); Observations From CSIF, GRACE, and CMS-Flux Were Withheld for the Prediction Period (2016–2018) While Retrieving Parameters During the Assimilation Stage (2010–2015)

	Full monthly da	ata r (RMSE)	Deseasonalized anomalies r (RMSE)		
	Assimilated NBP (2010–2015)	Predicted NBP (2016–2018)	Assimilated NBP (2010–2015)	Predicted NBP (2016–2018)	
NH South America	0.73* (0.19)	0.33* (0.31)	0.77* (0.12)	0.72* (0.15)	
SH South America	0.77* (0.27)	0.71* (0.31)	0.35* (0.17)	0.14 (0.17)	
NH Sub-Saharan Africa	0.93* (0.32)	0.96* (0.40)	0.42* (0.23)	0.44* (0.16)	
SH Africa	0.95* (0.34)	0.93* (0.45)	0.35* (0.25)	0.25 (0.21)	
Southeast Asia	0.54* (0.24)	0.18 (0.30)	0.68* (0.14)	0.63* (0.11)	
Australia	0.91* (0.14)	0.87* (0.16)	0.68* (0.13)	0.54* (0.11)	
Tropics	0.68* (0.10)	0.24 (0.14)	0.62* (0.06)	0.57* (0.05)	
Wet Tropics	0.62* (0.15)	0.35* (0.18)	0.59* (0.13)	0.48* (0.11)	
Dry Tropics	0.81* (0.11)	0.55* (0.16)	0.40* (0.06)	0.35* (0.05)	

Note. We then compared NBP between the observations (CMS-Flux) and the mean of the optimized posterior distribution for both the assimilation time and prediction time periods. We report correlation coefficients (r; the asterisks denote statistical significance with p-value < 0.05), and root mean squared error (RMSE, in units of gC m⁻² d⁻¹) for both the original monthly data and for annual averages.

3.2. Drivers of Tropical Carbon Flux Variability

On a pan-tropical scale, we find that the IAV of GPP_{def} anomalies ($\sigma\Delta$ GPP_{def}) is 52% greater than the IAV of GPP_{pot} anomalies ($\sigma\Delta$ GPP_{pot}) throughout 2001–2018 ($\sigma\Delta$ GPP_{def} = 1.98 PgC/yr, $\sigma\Delta$ GPP_{pot} = 1.30 PgC/yr; see Figure 3 for regional values). The dominance of GPP_{def} persists across both the dry tropics ($\sigma\Delta$ GPP_{def} is 26% greater than $\sigma\Delta$ GPP_{pot}), the wet tropics ($\sigma\Delta$ GPP_{def} is 94% greater than $\sigma\Delta$ GPP_{pot}), and four of six hemi-continental regions ($\sigma\Delta$ GPP_{def} is 22% and 11% smaller than $\sigma\Delta$ GPP_{pot} in Southern Hemisphere South America and Australia respectively, and 15%–89% larger across other regions). On both a pan-tropical and regional basis, de-seasonalized anomalies of GPP_{pot} and GPP_{def} are positively correlated (r = 0.22-0.53; p < 0.05; see Table S3 in Supporting Information S1), indicating that conditions of high photosynthetic potential (i.e., more sunlight and/or leaf area)

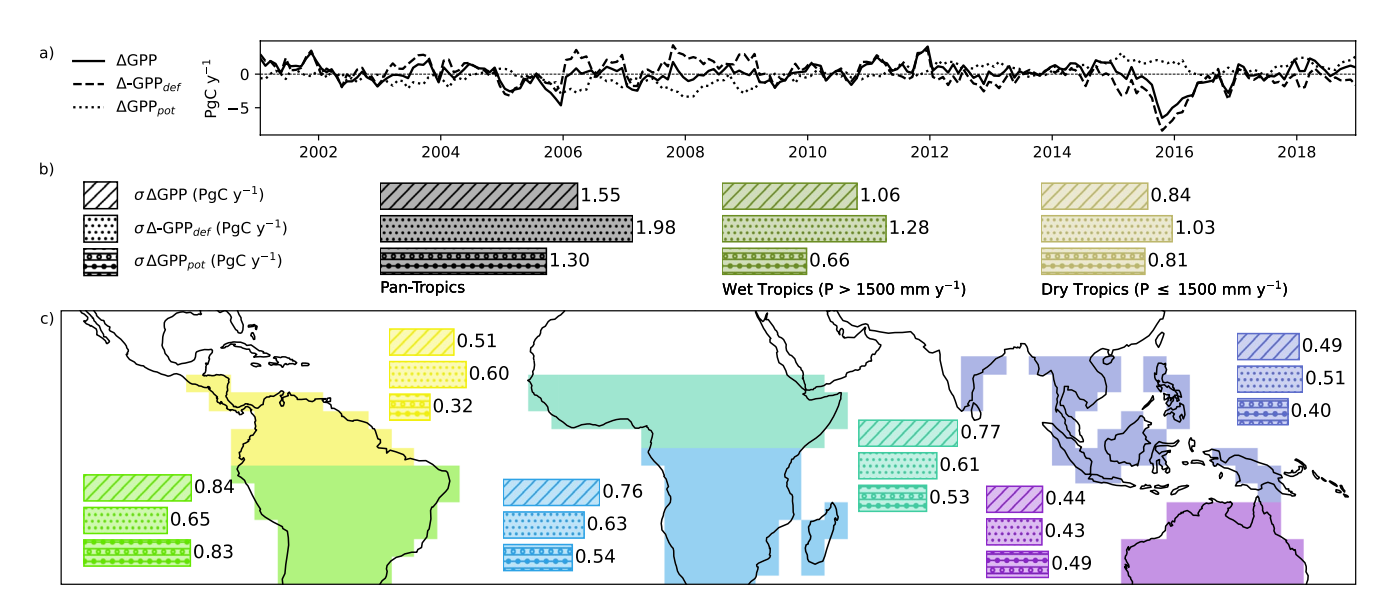


Figure 3. (a) Pan-tropically integrated monthly anomalies from the mean climatology of GPP (Δ GPP) and its two additive components (Δ GPP_{pot} and Δ -GPP_{def} see Equation 7). (b) Standard deviation of monthly anomalies of GPP (σ Δ GPP) and its two components (σ Δ GPP_{pot}, and σ Δ GPP_{def}) for the pan-tropics (the time series in a), the wet tropics, the dry tropics, and (c) six hemi-continental regions.

LEVINE ET AL. 9 of 17

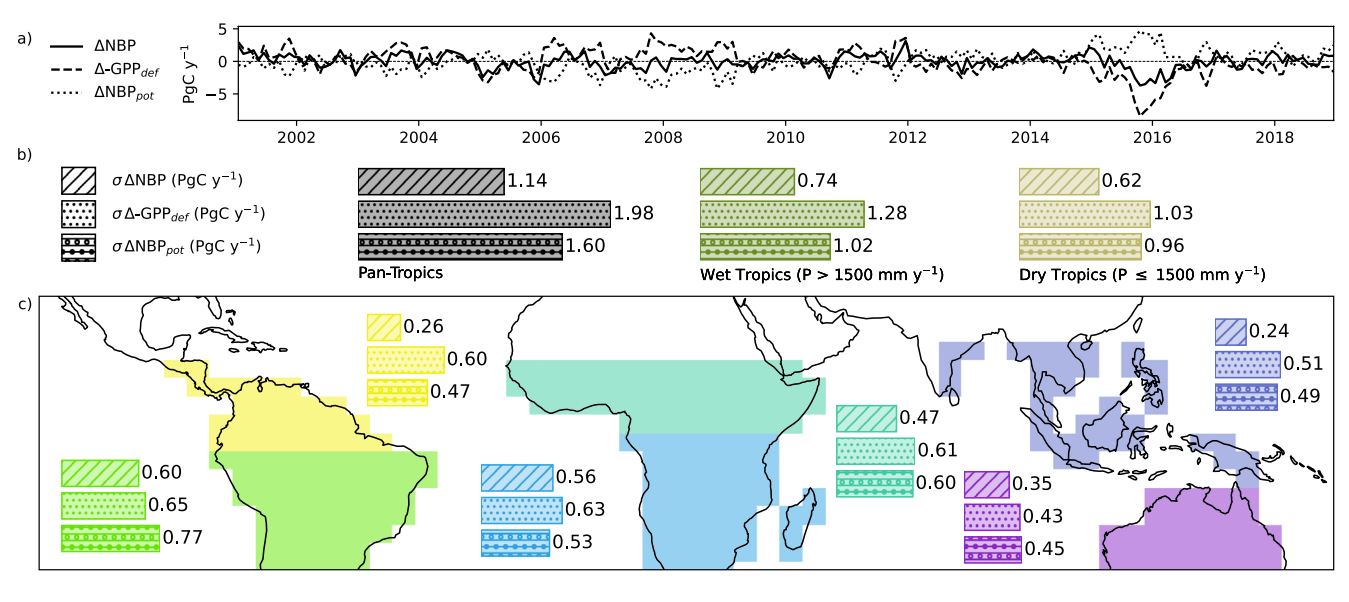


Figure 4. (a) Pan-tropically integrated monthly anomalies from the mean climatology of NBP (ΔNBP) and its two additive components (Δ NBP_{pot} and Δ -GPP_{def} see Equation 8). (b) Standard deviation of monthly anomalies of NBP (σ ΔNBP) and its two components (σ ΔNBP_{pot}, and σ ΔGPP_{def}) for the pan-tropics (the time series in a), the wet tropics, the dry tropics, and (c) six hemi-continental regions.

are associated with more water stress; these compensating interactions allow $\sigma\Delta GPP_{def}$ to exceed $\sigma\Delta GPP$ in some regions. The relative prominence of $\sigma\Delta GPP_{def}$ over $\sigma\Delta GPP_{pot}$ across the tropics—and within most individual regions—indicates that hydrologically imposed limitations to photosynthetic CO_2 uptake (GPP_{def}) are more highly variable on an inter-annual basis than the combined effects of radiation, temperature, and leaf area (GPP_{pot}) .

Extending the analysis to the net atmosphere-to-land CO_2 flux (NBP), the IAV of NBP $_{pot}$ ($\sigma\Delta$ NBP $_{pot}$) is generally greater than $\sigma\Delta$ GPP $_{pot}$, but less than $\sigma\Delta$ GPP $_{def}$ (Figure 4). $\sigma\Delta$ GPP $_{def}$ exceeds $\sigma\Delta$ NBP $_{pot}$ by 24% across the tropics as a whole, by 26% in the wet tropics, and by 7% in the dry tropics, and by 2%–39% across all hemi-continental regions. As with $\sigma\Delta$ GPP $_{pot}$, $\sigma\Delta$ NBP $_{pot}$ is greater than $\sigma\Delta$ GPP $_{def}$ in Southern Hemisphere South America and Australia (by 15% and 3%, respectively), while $\sigma\Delta$ GPP $_{def}$ exceeds $\sigma\Delta$ NBP $_{pot}$ in the other regions by 3%–28%. This indicates that with the exceptions of Southern Hemisphere South America and Australia, the IAV of water stress on GPP equals or exceeds the IAV of the combination of individual components comprising Δ NBP $_{pot}$ (namely Δ GPP $_{pot}$ and anomalies of fire and respiration fluxes). Furthermore, with the aforementioned regional exceptions, $\sigma\Delta$ GPP $_{def}$ is greater than the IAV of individual components of Δ NBP $_{pot}$ (see Tables S4–S6 in Supporting Information S1 for full variance-covariance matrices). Despite $\sigma\Delta$ NBP $_{pot}$ exceeding $\sigma\Delta$ GPP $_{pot}$ across the wet, dry, and pan-tropics, and half of the hemi-continental regions, $\sigma\Delta$ NBP is always less than $\sigma\Delta$ GPP. The low $\sigma\Delta$ NBP reflect compensating interactions between GPP $_{def}$ and NBP $_{pot}$ (r=0.49-0.92, p<0.05), which include the previously mentioned interactions between GPP $_{def}$ and GPP $_{pot}$ in addition to interactions between GPP $_{def}$ and respiration (see Tables S4–S6 in Supporting Information S1).

We find that the IAV of GPP^{vpd}_{def} ($\sigma\Delta\text{GPP}^{vpd}_{def}$) is generally larger than the IAV of GPP^{paw}_{def} ($\sigma\Delta\text{GPP}^{paw}_{def}$) across much of the tropics, indicating that the effects of atmospheric aridity are somewhat larger than the effects of soil moisture on $\sigma\Delta\text{GPP}_{def}$ (Figure 5). $\sigma\Delta\text{GPP}^{vpd}_{def}$ is 21% larger than $\sigma\Delta\text{GPP}^{paw}_{def}$ across the tropics as a whole, 33% larger in the wet tropics, and 6% larger in the dry tropics. Within the hemi-continental regions, $\sigma\Delta\text{GPP}^{paw}_{def}$ exceeds $\sigma\Delta\text{GPP}^{vpd}_{def}$ in Southern Hemisphere South America and Southern Hemisphere Africa by 18% and 48% respectively, while $\sigma\Delta\text{GPP}^{vpd}_{def}$ is larger than $\sigma\Delta\text{GPP}^{paw}_{def}$ in the other regions by 7%–45%. From a process standpoint, we find that the retrieved onset of GPP stress (β_{paw} < 1, see Figure 1) is typically at ≤30% of mean plant-available across hemi-continental regions and on a pantropical basis (Figure S9 in Supporting Information S1). In contrast, VPD-induced GPP stress (β_{vpd} < 1) span a broader range of VPD sensitivities; however, on a pantropical scale, we find that β_{vpd} declines in response to relative VPD changes are comparable across both the wet and dry tropics. Anomalies of GPP^{paw}_{def} and GPP^{vpd}_{def} are positively correlated (r = 0.09-0.65, p < 0.05), and the correlation is substantially greater in the wet tropics (0.65) than the dry tropics (0.32); this is consistent with previous work

LEVINE ET AL. 10 of 17

19449224, 2023, 12, Downloaded from https://agupubs.onlinelibrary.wiley.com/doi/10.1029/2023GB007702 by Stanford University, Wiley Online Library on [27/01/2024]. See the Term

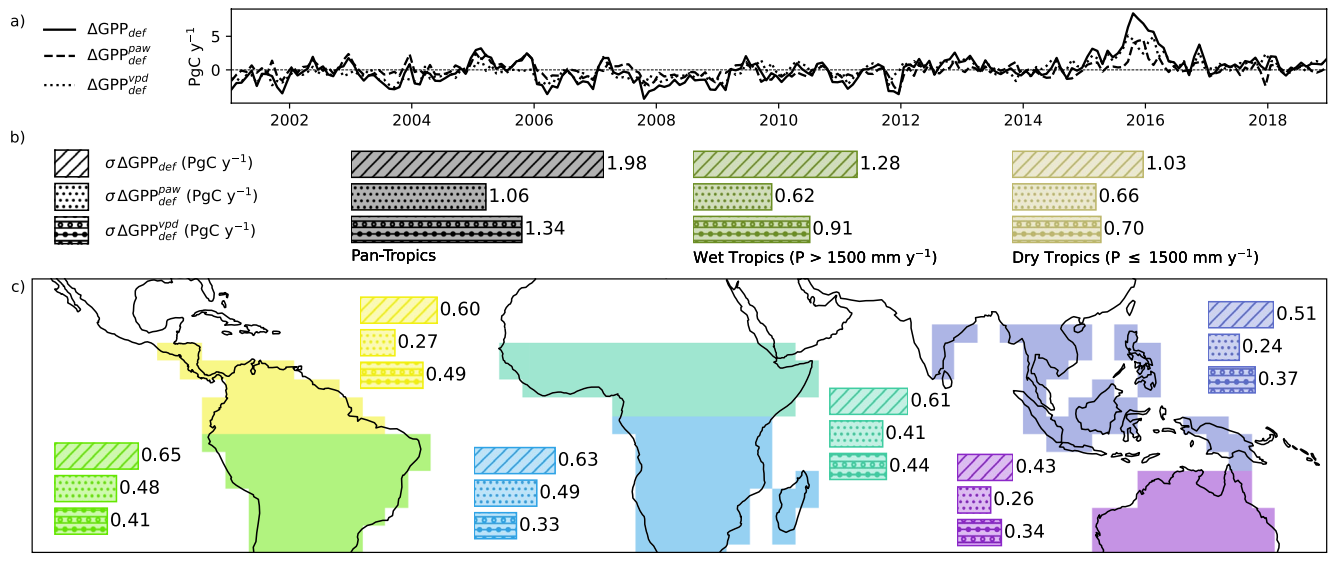


Figure 5. (a) Pan-tropically integrated monthly anomalies from the mean climatology of $GPP_{def}(\Delta GPP_{def})$ and its two additive components (ΔGPP_{def}^{vpd} and ΔGPP_{def}^{paw}) see Equation 9). (b) Standard deviation of monthly anomalies of $GPP_{def}(\sigma \Delta GPP_{def})$ and its two components ($\sigma \Delta GPP_{def}^{vpd}$, and $\sigma \Delta GPP_{def}^{paw}$) for the pan-tropics (the time series in a), the wet tropics, the dry tropics, and (c) six hemi-continental regions.

diagnosing positive correlations between soil moisture and atmospheric aridity (Green et al., 2019; Humphrey et al., 2021; Levine et al., 2019).

3.3. Water Stress in the Wet Tropics

Our finding that the IAV of GPP_{def} is greater than the IAV of GPP_{pot} in both the wet and dry regions (Figure 3) demonstrate that the IAV of gross terrestrial CO_2 uptake (GPP) in the tropics is dominated by hydrologically imposed limitations, with a relatively smaller contribution from downward radiation and ecosystem states. This dominance of water stress is reduced when considering the net CO_2 sink, but it still remains a prominent component of IAV, particularly in the wet tropics (Figure 4). Water supply (PAW) and demand (VPD) are both substantial drivers of water stress variability throughout the tropics, being roughly comparable in the dry tropics, but in the wet tropics, VPD limitations to GPP are more variable (Figure 5).

The importance of water stress in the wet tropics is surprising, given that evapotranspiration and photosynthesis in these areas is often thought to be limited by energy, rather than water (Baker et al., 2021; Claessen et al., 2019). Our results contrast with previous pan-tropical and global-scale analyses, which suggest semi-arid ecosystems are the largest contributor to the IAV of GPP (Y. Zhang et al., 2016) and net CO_2 fluxes (Ahlström et al., 2015; Fan et al., 2019; Piao et al., 2020; Poulter et al., 2014). While these efforts have used an array of models and observations to resolve water stress impacts on C fluxes, the differences are likely attributable to the absence of gridded top-down CO_2 fluxes and water constraints, which are ultimately key for resolving the spatial variability in ecosystem carbon-water interactions. Because we resolve the contributions of GPP_{def} in a spatially explicit manner, we are able to capture the spatial variability of ecosystem response to water stress in a manner that cannot be accomplished by parameterizations with plant functional types (Bassiouni et al., 2020; Bloom et al., 2016; Konings & Gentine, 2017). We also capture the spatial variability of the SIF-GPP relationship, which is driven by water availability (Chen et al., 2020).

The wet tropics in general have been a source of uncertainty among land modeling efforts (Huntzinger et al., 2017), and yet are increasingly highlighted as a key term in the interannual atmospheric CO₂ budget (Humphrey et al., 2018; J. Liu et al., 2017). Our assessment of water stress on NBP demonstrates that the instantaneous wet tropical water variability impacts on carbon cycling alone (0.75 PgC/y; see Figure 4; Table S2 in Supporting Information S1) amount to a substantial portion of the pantropical net carbon flux variability (0.95 PgC/y). Independent estimates of land carbon sink variations in wet tropical ecosystem responses to dry events (Bowman et al., 2017; Gatti et al., 2014) also support the inherent role of water stress in the wet tropics

LEVINE ET AL. 11 of 17

as a key regulator of the global land carbon sink. We note that the lagged impacts on NBP—mediated by decline in leaf area due to prolonged GPP decline, additional respiration due to increased leaf turnover/mortality and subsequent decomposition, and increased vulnerability to fire—may further enlarge the relative contribution of water stress on NBP. Querying the full spectrum of concurrent and lagged ecosystem responses to single water stress disturbances (Frank et al., 2015) or cumulative impacts of water stress events on aggregate lagged effects (Bloom et al., 2020) is therefore a necessary step to resolve the cumulative impact of water stress of the tropical land carbon sink.

3.4. Limitations and Future Directions

The magnitude of GPP_{pot} (Section 2.1) accounts for all non-water stress terms; in addition to temperature and radiation forcing, GPP_{pot} comprises of leaf-area phenology as well as host of underlying processes regulating photosynthesis, including species distribution and their phenological prominence, leaf-level photosynthetic efficiency, seasonal senescence in deciduous ecosystems, and mortality impacts on leaf area. We highlight that the perennial state of GPP_{pot} —which represent GPP values under non-arid conditions and are invariably not fully represented in the meteorological forcing record—is ultimately uncertain. However, as our analysis hinges on the variability (rather than the absolute values) of GPP_{pot} , we expect uncertainties on mean GPP_{pot} values to bear a secondary influence on our results.

The role of time-varying leaf area, however, is specifically a considerable source of GPP_{pot} temporal variability; across both wet and dry tropical ecosystems, we find that temporal GPP_{pot} variability is highly correlated with leaf area (5th–95th percentile of r values across all pixels span 0.41–0.95; p < 0.05; Figure S10 in Supporting Information S1). Given the important regional roles of GPP_{pot} —particularly in Southern Hemisphere South America and Australia where $\sigma\Delta GPP_{pot}$ IAV is greater than $\sigma\Delta GPP_{def}$ (Figure 3)—we identify the need to advance understanding of leaf area temporal dynamics, the associated process controls, and their impact on GPP. We note that while deciduous leaf area dynamics are represented in DALEC (Bloom & Williams, 2015), there are no explicit process representations of stress-induced leaf area senescence, which could ultimately lead to ambiguous or inaccurate attribution of GPP anomalies to GPP_{pot} and GPP_{def} where and when substantial leaf area changes take place. Ultimately, leveraging recent efforts resolving leaf area sensitivity to climate variability and soil water (Norton et al., 2023) provides a quantitative path forward for improving GPP_{pot} estimates and the subsequent attribution of GPP anomalies to GPP_{pot} and GPP_{def}

We highlight that the results presented in Section 3.2 may ultimately bear a substantial sensitivity to uncertainty choices prescribed for each observational data sets (see Data Availability Statement). Although uncertainty choices used in this study are broadly based on fundamental understanding of uncertainty for each observation type (Data Availability Statement; Table S1 in Supporting Information S1), we acknowledge that additional error characterizations, such as (a) unknown roles of error co-variances within or across observation types, (b) systematic errors in model-data consistency (Bloom et al., 2020), and (c) model structure and its impact on skill (Famiglietti et al., 2021), may ultimately benefit from more formal treatment or further exploration. In addition, while the model evaluation approach presented in Section 3.1 provides a broad assessment of hemi-continental and pantropical model skill (Tables 1 and 2)—where the model-data consistency in both assimilated and withheld carbon fluxes provides partial support for prescribed observation uncertainties (Famiglietti et al., 2021)—we nonetheless advocate for further and more systematic exploration on the role of uncertainty choices on future CARDAMOM carbon and water cycle inferences.

A limitation of our analysis is that we cannot fully account for the interactions between VPD and PAW resulting from land–atmosphere coupling (Green et al., 2019; Humphrey et al., 2021; Levine et al., 2019). Because VPD is part of the atmospheric forcing, it is unable to respond to variability in the prognostic PAW state. However, because PAW is constrained by observations from GRACE, the actual co-variability of PAW and VPD should be captured in our reanalysis. On the scale of individual plants, the limiting factor is hydraulic failure incurred when the water potential in xylem and leaf tissue becomes too low, which is a function of the water potential at both the roots and stomata. If plants do not sufficiently close stomata before atmospheric demand exceeds supply, they risk extremely negative leaf and xylem water potential, resulting in tissue damage. It has been hypothesized that individual plant species have evolved strategies for regulating the increased cost of PAW use due to increased VPD by decreasing stomatal conductance, thereby conserving water but limiting photosynthesis (Konings & Gentine, 2017; Massmann et al., 2019; Novick et al., 2019; Sperry et al., 2017). This has prompted

LEVINE ET AL. 12 of 17

suggestions that land surface models should incorporate hydraulic traits in parameterizations of plant responses to soil moisture and VPD in place of the simpler formulations most models have been using (Anderegg et al., 2019; Novick et al., 2019; Trugman et al., 2018). Our results suggest that plant responses to water supply and demand are likely both key processes in regulating tropical plant hydraulics. To advance process-level understanding of the role of plant hydraulics on the evolution of the tropical C balance, we therefore advocate for the advance of Bayesian model-data integration methods representing plant hydraulics explicitly (Y. Liu et al., 2020; Massoud et al., 2021) to include a comprehensive ensemble of satellite measurements including terrestrial water storage, fluorescence and CO₂ fluxes, and vegetation optical depth, among other ancillary ecosystem observations.

Linear scaling factors like β_{paw} and β_{vpd} have been widely used in land surface models to parameterize reductions in photosynthesis and transpiration due to water stress (Trugman et al., 2018; Verhoef & Egea, 2014), although the simplicity of this approach has been criticized in recent literature, which argues that plant hydraulic traits are better predictors of response to water stress (Trugman et al., 2019). In the work presented here, the parsimony of this formulation was a strength, as it minimized the number of parameters that we needed to constrain with our observational data. Furthermore, many of the criticisms of the approach are related to the limitations of PFT parameterizations. Instead, we optimized parameters independently for each grid cell, which would be impractical in a more complex trait-based model, and which allows us to capture the spatial variability of water use efficiency (Lin et al., 2015; J. Liu et al., 2021) and water stress thresholds (Bassiouni et al., 2020). To augment insight on the role of process representation on inferred GPP sensitivity, we advocate for further exploration of optimized CARDAMOM model parameters, their covariance, principal components of variability (Famiglietti et al., 2021) and the sensitivity of emergent GPP variability—and its attribution to individual process controls—to underlying parameter combinations and their associated uncertainties.

4. Summary and Implications

The ubiquity of water stress variability in the tropics (Figures 3 and 4) and the nearly equal variability of the instantaneous photosynthetic limitations (Figure 5) by PAW and VPD suggest that the tropical carbon cycle will respond strongly to future changes in both water supply and demand. In particular, precipitation supply across tropical ecosystems has varied considerably over the past two decades, while Earth System models predict that precipitation variability will increase throughout the remainder of the century (Pendergrass et al., 2017). Similarly, atmospheric water demand via VPD has been increasing over the past few decades (Barkhordarian et al., 2019; Yuan et al., 2019). Furthermore, soil moisture-atmosphere feedbacks have been identified as key co-mediating processes regulating both PAW and VPD (Green et al., 2019; Humphrey et al., 2021; Levine et al., 2019), suggesting that climate-driven trends of each one could intensify the response of the other.

Given that water supply and atmospheric demand each play a comparable role on water stress, our results further highlight the need to characterize the concurrent and lagged interactions between PAW and VPD. While water supply variability is fundamentally limited by precipitation and its legacy influence on soil water states, atmospheric water demand variability is an indirect result of concurrent anomalies of air temperature and moisture, which are in turn a result of atmospheric transport as well as concurrent evapotranspiration (Green et al., 2019; Humphrey et al., 2021; Levine et al., 2019). The feedback between VPD and PAW further highlights that wet and dry season climate shifts (Murray-Tortarolo et al., 2017) will exert compound influences on the magnitude and seasonality of GPP water stress. Further consideration of ecohydrological processes regulating stomatal conductance responses to demand and supply, including hydrologic plant traits (Y. Liu et al., 2020), isohydricity (Konings & Gentine, 2017), stomatal responses to elevated CO₂ (Swann & Koven, 2017), and rooting depth and soil traits (Massoud et al., 2021) will be critical for accurately resolving (a) the competing stresses on contemporary plant carbon uptake, and (b) the subsequent impacts of plant water stress on net land-atmosphere CO₂ flux in the coming decades. Finally, we speculate that evaluation of integrated GPP water stresses in Earth System models against data-constrained water stress mechanisms will be a critical step for benchmarking and improving joint water-carbon cycles and their role in the decadal land carbon sink projections.

Data Availability Statement

All data and code used in this work is publicly available. Code is available at the repository https://github.com/CARDAMOM-framework/CARDAMOM_v2.2. In Forcing data and Assimilation data, we account for all of the data we acquired, which would allow a complete replication of this work. In addition, we provide our

LEVINE ET AL. 13 of 17

CARDAMOM input files, in which all of the data has been regridded and aggregated to a common spatial and temporal resolution, which would allow our assimilation to be replicated without requiring any data acquisition. Finally, we provide the CARDAMOM output files, which would allow our analysis to be replicated without requiring the computationally expensive data assimilation. In the event this manuscript is accepted for publication, CARDAMOM input and output files will be on a public data repository with a digital object identifier. While undergoing review, these files will be furnished upon request to editors and external reviewers.

Forcing data: ERA-Interim re-analysis data sets were obtained from https://www.ecmwf.int/en/forecasts/data-set/ecmwf-reanalysis-interim (Berrisford et al., 2011). GFED4 burned area was obtained from https://dx.doi. org/10.3334/ORNLDAAC/1293 (Randerson et al., 2017). Atmospheric CO₂ concentrations were obtained from https://www.esrl.noaa.gov/gmd/ccgg/trends/gl_data.html (Dlugokencky & Tans, 2020).

Assimilation data: CMS-Flux data sets are available at http://cmsflux.jpl.nasa.gov. Atmospheric satellite-column CO₂ retrievals were obtained from the Atmospheric Carbon Observations from Space (ACOS) team for both GOSAT (version 7.3) and OCO-2 (version 9) using a common algorithm (Crisp et al., 2012). Prior ecosystem fluxes are derived from CARDAMOM (Bloom et al., 2016), ocean fluxes from the ECCO-Darwin Model (Carroll et al., 2020), and fossil fuel from the Open-source Data Inventory for Anthropogenic CO₂ (ODIAC) 2018 (Oda et al., 2018).

GRACE terrestrial water storage anomalies were obtained from http://dx.doi.org/10.5067/TEMSC-OCL05 (Wiese et al., 2016). CSIF data were acquired from http://dx.doi.org/10.17605/OSF.IO/8XQY6 (Y. Zhang et al., 2018). MODIS LAI data were obtained from https://doi.org/10.5067/MODIS/MODIS/MOD15A2H.006 (Myneni et al., 2015). Biomass is available from Sassan Saatchi (sasan.s.saatchi@jpl.nasa.gov) upon reasonable request (Saatchi et al., 2011). HWSD soil organic carbon data was obtained from https://dx.doi.org/10.2788/13267 (Hiederer & Köchy, 2012). Biomass burning CO fluxes data was obtained from https://doi.org/10.26024/r1r2-6620 (Bloom et al., 2019). FLUXCOM data sets were obtained from http://www.fluxcom.org/CF-Download/ (Jung et al., 2019).

Acknowledgments

The research was carried out at the Jet Propulsion Laboratory, California Institute of Technology, under a contract with the National Aeronautics and Space Administration. ML was supported by the NASA Postdoctoral Program, administered by Universities Space Research Association under contract with NASA. AGK was supported by NSF DEB-1942133. PAL, AAB, AGK, and VM were also supported by the NASA Carbon Cycle Science program. PAL, JTR, and VM were supported by NASA GRACE-FO science team. This research was supported by two NASA Earth Sciences Grants (no. NNH16ZDA001N-IDS and NNH20ZDA001N-CARBON).

References

- Ahlström, A., Canadell, J. G., Schurgers, G., Wu, M., Berry, J. A., Guan, K., & Jackson, R. B. (2017). Hydrologic resilience and amazon productivity. *Nature Communications*, 8(1), 387. https://doi.org/10.1038/s41467-017-00306-z
- Ahlström, A., Raupach, M. R., Schurgers, G., Smith, B., Arneth, A., Jung, M., et al. (2015). The dominant role of semi-arid ecosystems in the trend and variability of the land CO₂ sink. *Science*, 348(6237), 895–899. https://doi.org/10.1126/science.aaa1668
- Anderegg, W. R. L., Trugman, A. T., Bowling, D. R., Salvucci, G., & Tuttle, S. E. (2019). Plant functional traits and climate influence drought intensification and land–atmosphere feedbacks. *Proceedings of the National Academy of Sciences of the United States of America*, 116(28), 14071–14076. https://doi.org/10.1073/pnas.1904747116
- Avitabile, V., Herold, M., Heuvelink, G. B. M., Lewis, S. L., Phillips, O. L., Asner, G. P., et al. (2016). An integrated pan-tropical biomass map using multiple reference datasets. *Global Change Biology*, 22(4), 1406–1420. https://doi.org/10.1111/gcb.13139
- Baker, J. C. A., Garcia-Carreras, L., Buermann, W., de Souza, D. C., Marsham, J. H., Kubota, P. Y., et al. (2021). Robust amazon precipitation projections in climate models that capture realistic land–atmosphere interactions. *Environmental Research Letters*, 16(7), 074002. https://doi.org/10.1088/1748-9326/abfb2e
- Barkhordarian, A., Bowman, K. W., Cressie, N., Jewell, J., & Liu, J. (2021). Emergent constraints on tropical atmospheric aridity—Carbon feedbacks and the future of carbon sequestration. *Environmental Research Letters*, 16(11), 114008. https://doi.org/10.1088/1748-9326/ac2ce8 Barkhordarian, A., Saatchi, S. S., Behrangi, A., Loikith, P. C., & Mechoso, C. R. (2019). A recent systematic increase in vapor pressure deficit over tropical South America. *Scientific Reports*, 9(1), 15331. https://doi.org/10.1038/s41598-019-51857-8
- Bassiouni, M., Good, S. P., Still, C. J., & Higgins, C. W. (2020). Plant water uptake thresholds inferred from satellite soil moisture. *Geophysical Research Letters*, 47(7), e2020GL087077. https://doi.org/10.1029/2020GL087077
- Berrisford, P., Dee, D., Poli, P., Brugge, R., Fielding, M., Fuentes, M., et al. (2011). The ERA-Interim archive version 2.0. European Centre for Medium-Range Weather Forecasts, (1), 23. Retrieved from https://www.ecmwf.int/node/8174
- Bi, J., Knyazikhin, Y., Choi, S., Park, T., Barichivich, J., Ciais, P., et al. (2015). Sunlight mediated seasonality in canopy structure and photosynthetic activity of amazonian rainforests. *Environmental Research Letters*, 10(6), 064014. https://doi.org/10.1088/1748-9326/10/6/064014
- Bloom, A. A., Bowman, K. W., Liu, J., Konings, A. G., Worden, J. R., Parazoo, N. C., et al. (2020). Lagged effects regulate the inter-annual variability of the tropical carbon balance. *Biogeosciences*, 17(24), 6393–6422. https://doi.org/10.5194/bg-17-6393-2020
- Bloom, A. A., Exbrayat, J.-F., van der Velde, I. R., Feng, L., & Williams, M. (2016). The decadal state of the terrestrial carbon cycle: Global retrievals of terrestrial carbon allocation, pools, and residence times. *Proceedings of the National Academy of Sciences of the United States of America*, 113(5), 1285–1290. https://doi.org/10.1073/pnas.1515160113
- Bloom, A. A., Jiang, Z., & Worden, H. (2019). Global carbon monoxide (CO) flux estimates for 2001-2015. version 1.0. https://doi.org/10.26024/
- Bloom, A. A., & Williams, M. (2015). Constraining ecosystem carbon dynamics in a data-limited world: Integrating ecological "common sense" in a model–data fusion framework. *Biogeosciences*, 12(5), 1299–1315. https://doi.org/10.5194/bg-12-1299-2015
- Bonal, D., Bosc, A., Stéphane, P., Goret, J.-Y., Benoît, B., Gross, P., et al. (2008). Impact of severe dry season on net ecosystem exchange in the Neotropical rainforest of French Guiana. *Global Change Biology*, 14(8), 1917–1933. https://doi.org/10.1111/j.1365-2486.2008.01610.x
- Bonan, G. B., Williams, M., Fisher, R. A., & Oleson, K. W. (2014). Modeling stomatal conductance in the Earth system: Linking leaf water-use efficiency and water transport along the soil–plant–atmosphere continuum. *Geoscientific Model Development*, 7(5), 2193–2222. https://doi.org/10.5194/gmd-7-2193-2014

LEVINE ET AL. 14 of 17



Global Biogeochemical Cycles

- 10.1029/2023GB007702
- Bowman, K. W., Liu, J., Bloom, A. A., Parazoo, N. C., Lee, M., Jiang, Z., et al. (2017). Global and Brazilian carbon response to El Niño Modoki 2011–2010. Earth and Space Science, 4(10), 637–660. https://doi.org/10.1002/2016EA000204
- Carroll, D., Menemenlis, D., Adkins, J. F., Bowman, K. W., Brix, H., Dutkiewicz, S., et al. (2020). The ECCO-Darwin data-assimilative global ocean biogeochemistry model: Estimates of seasonal to multi-decadal surface ocean pCO₂ and air-sea CO₂ flux. *Journal of Advances in Modeling Earth Systems*, 12(10), e2019MS001888. https://doi.org/10.1029/2019MS001888
- Chen, A., Mao, J., Ricciuto, D., Xiao, J., Frankenberg, C., Li, X., et al. (2020). Moisture availability mediates the relationship between terrestrial gross primary production and solar-induced chlorophyll fluorescence: Insights from global-scale variations. *Global Change Biology*, 00(6), 1–13. https://doi.org/10.1111/gcb.15373
- Claessen, J., Molini, A., Martens, B., Detto, M., Demuzere, M., & Miralles, D. G. (2019). Global biosphere–climate interaction: A causal appraisal of observations and models over multiple temporal scales. *Biogeosciences*, 16(24), 4851–4874. https://doi.org/10.5194/bg-16-4851-2019
- Cox, P. M., Pearson, D., Booth, B. B., Friedlingstein, P., Huntingford, C., Jones, C. D., & Luke, C. M. (2013). Sensitivity of tropical carbon to climate change constrained by carbon dioxide variability. *Nature*, 494(7437), 341–344. https://doi.org/10.1038/nature11882
- Crisp, D., Fisher, B. M., O'Dell, C., Frankenberg, C., Basilio, R., Bösch, H., et al. (2012). The ACOS CO₂ retrieval algorithm–part II: Global X CO₂ data characterization. *Atmospheric Measurement Techniques*, 5(4), 687–707. https://doi.org/10.5194/amt-5-687-2012
- Dlugokencky, E. J., & Tans, P. P. (2020). Trends in atmospheric carbon dioxide. Retrieved from https://gml.noaa.gov/ccgg/trends/global.html Famiglietti, C. A., Smallman, T. L., Levine, P. A., Flack-Prain, S., Quetin, G. R., Meyer, V., et al. (2021). Optimal model complexity for terrestrial carbon cycle prediction. *Biogeosciences*, 18(8), 2727–2754. https://doi.org/10.5194/bg-18-2727-2021
- Fan, L., Wigneron, J.-P., Ciais, P., Chave, J., Brandt, M., Fensholt, R., et al. (2019). Satellite-observed pantropical carbon dynamics. *Nature Plants*, 5(9), 944–951. https://doi.org/10.1038/s41477-019-0478-9
- Frank, D., Reichstein, M., Bahn, M., Thonicke, K., Frank, D., Mahecha, M. D., et al. (2015). Effects of climate extremes on the terrestrial carbon cycle: Concepts, processes and potential future impacts. *Global Change Biology*, 21(8), 2861–2880. https://doi.org/10.1111/gcb.12916
- Gatti, L. V., Gloor, M., Miller, J. B., Doughty, C. E., Malhi, Y., Domingues, L. G., et al. (2014). Drought sensitivity of Amazonian carbon balance revealed by atmospheric measurements. *Nature*, 506(7486), 76–80. https://doi.org/10.1038/nature12957
- Green, J. K., Berry, J., Ciais, P., Zhang, Y., & Gentine, P. (2020). Amazon rainforest photosynthesis increases in response to atmospheric dryness. Science Advances, 6(47). https://doi.org/10.1126/sciadv.abb7232
- Green, J. K., Seneviratne, S. I., Berg, A. M., Findell, K. L., Hagemann, S., Lawrence, D. M., & Gentine, P. (2019). Large influence of soil moisture on long-term terrestrial carbon uptake. *Nature*, 565(7740), 476–479. https://doi.org/10.1038/s41586-018-0848-x
- Grossiord, C., Buckley, T. N., Cernusak, L. A., Novick, K. A., Poulter, B., Siegwolf, R. T. W., et al. (2020). Plant responses to rising vapor pressure deficit. Nav. Phytologist. 226(6), 1550, 1566. https://doi.org/10.1111/pnb.16485
- sure deficit. New Phytologist, 226(6), 1550–1566. https://doi.org/10.1111/nph.16485
 Hiederer, R., & Köchy, M. (2012). Global soil organic carbon estimates and the harmonized world soil database. https://doi.org/10.2788/13267
- Humphrey, V., Berg, A., Ciais, P., Gentine, P., Jung, M., Reichstein, M., et al. (2021). Soil moisture–atmosphere feedback dominates land carbon uptake variability. *Nature*, 592(7852), 65–69. https://doi.org/10.1038/s41586-021-03325-5
- Humphrey, V., Zscheischler, J., Ciais, P., Gudmundsson, L., Sitch, S., & Seneviratne, S. I. (2018). Sensitivity of atmospheric CO₂ growth rate to observed changes in terrestrial water storage. *Nature*, 560(7720), 628–631. https://doi.org/10.1038/s41586-018-0424-4
- Huntzinger, D. N., Michalak, A. M., Schwalm, C., Ciais, P., King, A. W., Fang, Y., et al. (2017). Uncertainty in the response of terrestrial carbon sink to environmental drivers undermines carbon-climate feedback predictions. Scientific Reports, 7(1), 4765. https://doi.org/10.1038/s41598-017-03818-2
- Jackson, R. B., Lajtha, K., Crow, S. E., Hugelius, G., Kramer, M. G., & Piñeiro, G. (2017). The ecology of soil carbon: Pools, vulner-abilities, and biotic and abiotic controls. Annual Review of Ecology, Evolution, and Systematics, 48(1), 419–445. https://doi.org/10.1146/annurev-ecolsys-112414-054234
- Jones, C. D., Collins, M., Cox, P. M., & Spall, S. A. (2001). The carbon cycle response to ENSO: A coupled climate-carbon cycle model study. Journal of Climate, 14(21), 4113-4129. https://doi.org/10.1175/1520-0442(2001)014(4113:TCCRTE)2.0.CO;2
- Jung, M., Koirala, S., Weber, U., Ichii, K., Gans, F., Camps-Valls, G., et al. (2019). The fluxcom ensemble of global land-atmosphere energy fluxes. Scientific Data, 6(1), 74. https://doi.org/10.1038/s41597-019-0076-8
- Jung, M., Reichstein, M., Schwalm, C. R., Huntingford, C., Sitch, S., Ahlström, A., et al. (2017). Compensatory water effects link yearly global land CO₂ sink changes to temperature. *Nature*, 541(7638), 516–520. https://doi.org/10.1038/nature20780
- Jung, M., Schwalm, C., Migliavacca, M., Walther, S., Camps-Valls, G., Koirala, S., et al. (2020). Scaling carbon fluxes from eddy covariance sites to globe: Synthesis and evaluation of the fluxcom approach. *Biogeosciences*, 17(5), 1343–1365. https://doi.org/10.5194/bg-17-1343-2020
- Keeling, C. D., Whorf, T. P., Wahlen, M., & van der Plichtt, J. (1995). Interannual extremes in the rate of rise of atmospheric carbon dioxide since 1980. *Nature*, 375(6533), 666–670. https://doi.org/10.1038/375666a0
- Köchy, M., Hiederer, R., & Freibauer, A. (2015). Global distribution of soil organic carbon—Part 1: Masses and frequency distributions of SOC stocks for the tropics, permafrost regions, wetlands, and the world. Soil, 1(1), 351–365. https://doi.org/10.5194/soil-1-351-2015
- Konings, A. G., & Gentine, P. (2017). Global variations in ecosystem-scale isohydricity. Global Change Biology, 23(2), 891–905. https://doi.org/10.1111/gcb.13389
- Leuning, R. (1995). A critical appraisal of a combined stomatal-photosynthesis model for C3 plants. *Plant, Cell and Environment*, 18(4), 339–355. https://doi.org/10.1111/j.1365-3040.1995.tb00370.x
- Levine, P. A., Randerson, J. T., Chen, Y., Pritchard, M. S., Xu, M., & Hoffman, F. M. (2019). Soil moisture variability intensifies and prolongs eastern Amazon temperature and carbon cycle response to El Niño–Southern Oscillation. *Journal of Climate*, 32(4), 1273–1292. https://doi.org/10.1175/JCLI-D-18-0150.1
- Lin, Y.-S., Medlyn, B. E., Duursma, R. A., Prentice, I. C., Wang, H., Baig, S., et al. (2015). Optimal stomatal behavior around the world. *Nature Climate Change*, 5(5), 459–464. https://doi.org/10.1038/nclimate2550
- Liu, J., Baskaran, L., Bowman, K., Schimel, D., Bloom, A. A., Parazoo, N. C., et al. (2021). Carbon monitoring system flux net biosphere exchange 2020 (CMS-Flux NBE 2020). Earth System Science Data, 13(2), 299–330. https://doi.org/10.5194/essd-13-299-2021
- Liu, J., Bowman, K., Lee, M., Henze, D., Bousserez, N., Brix, H., et al. (2014). Carbon monitoring system flux estimation and attribution: Impact of ACOS-GOSAT XCO2 sampling on the inference of terrestrial biospheric sources and sinks. *Tellus B: Chemical and Physical Meteorology*, 66(0), 22486. https://doi.org/10.3402/tellusb.v66.22486
- Liu, J., Bowman, K. W., Schimel, D. S., Parazoo, N. C., Jiang, Z., Lee, M., et al. (2017). Contrasting carbon cycle responses of the tropical continents to the 2015–2016 El Niño. *Science*, 358(6360), eaam5690. https://doi.org/10.1126/science.aam5690
- Liu, Y., Kumar, M., Katul, G. G., Feng, X., & Konings, A. G. (2020). Plant hydraulics accentuates the effect of atmospheric moisture stress on transpiration. *Nature Climate Change*, 10(7), 691–695. https://doi.org/10.1038/s41558-020-0781-5
- MacBean, N., Maignan, F., Bacour, C., Lewis, P., Peylin, P., Guanter, L., et al. (2018). Strong constraint on modelled global carbon uptake using solar-induced chlorophyll fluorescence data. Scientific Reports, 8(1), 1973. https://doi.org/10.1038/s41598-018-20024-w

LEVINE ET AL. 15 of 17

- Madani, N., Kimball, J. S., Parazoo, N. C., Ballantyne, A. P., Tagesson, T., Jones, L. A., et al. (2020). Below-surface water mediates the response of African forests to reduced rainfall. *Environmental Research Letters*, 15(3), 034063. https://doi.org/10.1088/1748-9326/ab724a
- Massmann, A., Gentine, P., & Lin, C. (2019). When does vapor pressure deficit drive or reduce evapotranspiration? *Journal of Advances in Modeling Earth Systems*, 11(10), 3305–3320. https://doi.org/10.1029/2019MS001790
- Massoud, E. C., Bloom, A. A., Longo, M., Reager, J. T., Levine, P. A., & Worden, J. R. (2021). Information content of soil hydrology in the amazon as informed by grace. Hydrology and Earth System Sciences Discussions, 2021, 1–28. https://doi.org/10.5194/hess-2021-104
- Murray-Tortarolo, G., Jaramillo, V. J., Maass, M., Friedlingstein, P., & Sitch, S. (2017). The decreasing range between dry- and wet-season precipitation over land and its effect on vegetation primary productivity. *PLoS One*, 12(12), 1–11. https://doi.org/10.1371/journal.pone.0190304
- Myneni, R., Knyazikhin, Y., & Park, T. (2015). MOD15A2H MODIS/Terra leaf area Index/FPAR 8-Day l4 global 500m SIN grid v006. https://doi.org/10.5067/MODIS/MODIS/A2H.006
- Mystakidis, S., Davin, E. L., Gruber, N., & Seneviratne, S. I. (2016). Constraining future terrestrial carbon cycle projections using observation-based water and carbon flux estimates. Global Change Biology, 22(6), 2198–2215. https://doi.org/10.1111/gcb.13217
- Norton, A. J., Bloom, A. A., Parazoo, N. C., Levine, P. A., Ma, S., Braghiere, R. K., & Smallman, T. L. (2023). Improved process representation of leaf phenology significantly shifts climate sensitivity of ecosystem carbon balance. *Biogeosciences*, 20(12), 2455–2484. https://doi.org/10.5194/bg-20-2455-2023
- Novick, K. A., Ficklin, D. L., Stoy, P. C., Williams, C. A., Bohrer, G., Oishi, A. C., et al. (2016). The increasing importance of atmospheric demand for ecosystem water and carbon fluxes. *Nature Climate Change*, 6(11), 1023–1027. https://doi.org/10.1038/nclimate3114
- Novick, K. A., Konings, A. G., & Gentine, P. (2019). Beyond soil water potential: An expanded view on isohydricity including land–atmosphere interactions and phenology. *Plant, Cell and Environment*, 42(6), 1802–1815. https://doi.org/10.1111/pce.13517
- Oda, T., Maksyutov, S., & Andres, R. J. (2018). The open-source data inventory for anthropogenic CO₂, version 2016 (ODIAC2016): A global monthly fossil fuel CO₂ gridded emissions data product for tracer transport simulations and surface flux inversions. *Earth System Science Data*, 10(1), 87–107. https://doi.org/10.5194/essd-10-87-2018
- Palmer, P. I., Feng, L., Baker, D., Chevallier, F., Bösch, H., & Somkuti, P. (2019). Net carbon emissions from African biosphere dominate pan-tropical atmospheric CO₂ signal. *Nature Communications*, 10(1), 3344. https://doi.org/10.1038/s41467-019-11097-w
- Pendergrass, A. G., Knutti, R., Lehner, F., Deser, C., & Sanderson, B. M. (2017). Precipitation variability increases in a warmer climate. *Scientific Reports*, 7(1), 17966. https://doi.org/10.1038/s41598-017-17966-y
- Piao, S., Wang, X., Wang, K., Li, X., Bastos, A., Canadell, J. G., et al. (2020). Interannual variation of terrestrial carbon cycle: Issues and perspectives. Global Change Biology, 26(1), 300–318. https://doi.org/10.1111/gcb.14884
- Poulter, B., Frank, D., Ciais, P., Myneni, R. B., Andela, N., Bi, J., et al. (2014). Contribution of semi-arid ecosystems to interannual variability of the global carbon cycle. *Nature*, 509(7502), 600–603. https://doi.org/10.1038/nature13376
- Qian, H., Joseph, R., & Zeng, N. (2008). Response of the terrestrial carbon cycle to the El Niño-Southern Oscillation. *Tellus B: Chemical and Physical Meteorology*, 60(4), 537–550. https://doi.org/10.1111/j.1600-0889.2008.00360.x
- Quetin, G. R., Bloom, A. A., Bowman, K. W., & Konings, A. G. (2020). Carbon flux variability from a relatively simple ecosystem model with assimilated data is consistent with terrestrial biosphere model estimates. *Journal of Advances in Modeling Earth Systems*, 12(3), e2019MS001889. https://doi.org/10.1029/2019MS001889
- Randerson, J. T., van der Werf, G. R., Giglio, L., Collatz, G. J., & Kasibhatla, P. S. (2017). Global fire emissions database, version 4.1 (GFEDV4). ORNL Distributed Active Archive Center. https://doi.org/10.3334/ORNLDAAC/1293
- Rayner, P. J., Law, R. M., Allison, C. E., Francey, R. J., Trudinger, C. M., & Pickett-Heaps, C. (2008). Interannual variability of the global carbon cycle (1992–2005) inferred by inversion of atmospheric CO_2 and $\delta^{13}CO_2$ measurements. *Global Biogeochemical Cycles*, 22(3). https://doi.org/10.1029/2007GB003068
- Saatchi, S. S., Harris, N. L., Brown, S., Lefsky, M., Mitchard, E. T. A., Salas, W., et al. (2011). Benchmark map of forest carbon stocks in tropical regions across three continents. *Proceedings of the National Academy of Sciences of the United States of America*, 108(24), 9899–9904. https://doi.org/10.1073/pnas.1019576108
- Saatchi, S. S., Longo, M., Xu, L., Yang, Y., Abe, H., André, M., et al. (2021). Detecting vulnerability of humid tropical forests to multiple stress-ors. *One Earth*, 4(7), 988–1003. https://doi.org/10.1016/j.oneear.2021.06.002
- Sperry, J. S., Venturas, M. D., Anderegg, W. R. L., Mencuccini, M., Mackay, D. S., Wang, Y., & Love, D. M. (2017). Predicting stomatal responses to the environment from the optimization of photosynthetic gain and hydraulic cost. *Plant, Cell and Environment*, 40(6), 816–830. https://doi.org/10.1111/pce.12852
- Stephenson, N. (1998). Actual evapotranspiration and deficit: Biologically meaningful correlates of vegetation distribution across spatial scales. Journal of Biogeography, 25(5), 855–870. https://doi.org/10.1046/j.1365-2699.1998.00233.x
- Sulman, B. N., Roman, D. T., Yi, K., Wang, L., Phillips, R. P., & Novick, K. A. (2016). High atmospheric demand for water can limit forest carbon uptake and transpiration as severely as dry soil. *Geophysical Research Letters*, 43(18), 9686–9695. https://doi.org/10.1002/2016GL069416
- Swann, A. L. S., & Koven, C. D. (2017). A direct estimate of the seasonal cycle of evapotranspiration over the Amazon basin. *Journal of Hydrometeorology*, 18(8), 2173–2185. https://doi.org/10.1175/JHM-D-17-0004.1
- Trugman, A. T., Anderegg, L. D. L., Sperry, J. S., Wang, Y., Venturas, M., & Anderegg, W. R. L. (2019). Leveraging plant hydraulics to yield predictive and dynamic plant leaf allocation in vegetation models with climate change. *Global Change Biology*, 25(12), 4008–4021. https://doi.org/10.1111/gcb.14814
- Trugman, A. T., Medvigy, D., Mankin, J. S., & Anderegg, W. R. L. (2018). Soil moisture stress as a major driver of carbon cycle uncertainty. Geophysical Research Letters, 45(13), 6495–6503. https://doi.org/10.1029/2018GL078131
- Verhoef, A., & Egea, G. (2014). Modeling plant transpiration under limited soil water: Comparison of different plant and soil hydraulic parameterizations and preliminary implications for their use in land surface models. *Agricultural and Forest Meteorology*, 191, 22–32. https://doi.org/10.1016/j.agrformet.2014.02.009
- Wang, J., Zeng, N., & Wang, M. (2016). Interannual variability of the atmospheric CO₂ growth rate: Roles of precipitation and temperature. Biogeosciences, 13(8), 2339–2352. https://doi.org/10.5194/bg-13-2339-2016
- Wang, W., Ciais, P., Nemani, R. R., Canadell, J. G., Piao, S., Sitch, S., et al. (2013). Variations in atmospheric CO₂ growth rates coupled with tropical temperature. *Proceedings of the National Academy of Sciences of the United States of America*, 110(32), 13061–13066. https://doi.org/10.1073/pnas.1219683110
- Wang, X., Piao, S., Ciais, P., Friedlingstein, P., Myneni, R. B., Cox, P., et al. (2014). A two-fold increase of carbon cycle sensitivity to tropical temperature variations. *Nature*, 506(7487), 212–215. https://doi.org/10.1038/nature12915
- Wiese, D. N., Landerer, F. W., & Watkins, M. M. (2016). Quantifying and reducing leakage errors in the JPL RL05M GRACE mascon solution. Water Resources Research, 52(9), 7490–7502. https://doi.org/10.1002/2016WR019344

LEVINE ET AL. 16 of 17

- Williams, M., Rastetter, E. B., Fernandes, D. N., Goulden, M. L., Shaver, G. R., & Johnson, L. C. (1997). Predicting gross primary productivity in terrestrial ecosystems. *Ecological Applications*, 7(3), 882–894. https://doi.org/10.1890/1051-0761(1997)007[0882:PGPPIT]2.0.CO;2
- Williams, M., Schwarz, P. A., Law, B. E., Irvine, J., & Kurpius, M. R. (2005). An improved analysis of forest carbon dynamics using data assimilation. Global Change Biology, 11(1), 89–105. https://doi.org/10.1111/j.1365-2486.2004.00891.x
- Worden, J. R., Bloom, A. A., Pandey, S., Jiang, Z., Worden, H. M., Walker, T. W., et al. (2017). Reduced biomass burning emissions reconcile conflicting estimates of the post-2006 atmospheric methane budget. *Nature Communications*, 8(1), 2227. https://doi.org/10.1038/s41467-017-02246-0
- Worden, J. R., Saatchi, S., Keller, M., Bloom, A. A., Liu, J., Parazoo, N., et al. (2021). Satellite observations of the tropical terrestrial carbon balance and interactions with the water cycle during the 21st century. *Reviews of Geophysics*, 59(1), e2020RG000711. https://doi.org/10.1029/2020RG000711
- Yang, Y., Bloom, A. A., Ma, S., Levine, P., Norton, A., Parazoo, N. C., et al. (2021). Cardamom-fluxval version 1.0: A fluxnet-based validation system for cardamom carbon and water flux estimates. Geoscientific Model Development Discussions, 1–25. https://doi.org/10.5194/gmd-2021-190
- Yang, Y., Saatchi, S. S., Xu, L., Yu, Y., Choi, S., Phillips, N., et al. (2018). Post-drought decline of the amazon carbon sink. Nature Communications, 9(1), 3172. https://doi.org/10.1038/s41467-018-05668-6
- Yin, Y., Bloom, A. A., Worden, J., Saatchi, S., Yang, Y., Williams, M., et al. (2020). Fire decline in dry tropical ecosystems enhances decadal land carbon sink. *Nature Communications*, 11(1), 1900. https://doi.org/10.1038/s41467-020-15852-2
- Yuan, W., Zheng, Y., Piao, S., Ciais, P., Lombardozzi, D., Wang, Y., et al. (2019). Increased atmospheric vapor pressure deficit reduces global vegetation growth. *Science Advances*, 5(8). https://doi.org/10.1126/sciadv.aax1396
- Zeng, N., Mariotti, A., & Wetzel, P. (2005). Terrestrial mechanisms of interannual CO₂ variability. Global Biogeochemical Cycles, 19(1), GB1016. https://doi.org/10.1029/2004GB002273
- Zhang, A., & Jia, G. (2020). ENSO-driven reverse coupling in interannual variability of pantropical water availability and global atmospheric CO₂ growth rate. Environmental Research Letters, 15(3), 034006. https://doi.org/10.1088/1748-9326/ab66cc
- Zhang, Y., Joiner, J., Alemohammad, S. H., Zhou, S., & Gentine, P. (2018). A global spatially contiguous solar-induced fluorescence (CSIF) dataset using neural networks. Biogeosciences, 15(19), 5779–5800. https://doi.org/10.5194/bg-15-5779-2018
- Zhang, Y., Xiao, X., Guanter, L., Zhou, S., Ciais, P., Joiner, J., et al. (2016). Precipitation and carbon-water coupling jointly control the interannual variability of global land gross primary production. *Scientific Reports*, 6(1), 39748. https://doi.org/10.1038/srep39748

LEVINE ET AL. 17 of 17